Influence of Impeller Shroud Forces on Turbopump Rotor Dynamics

J. P. Williams
Rockwell Space Operations Company,
600 Gemini, R20-B,
Houston, TX 77058

D. W. Childs
Department of Mechanical Engineering,
Texas A&M University,
College Station, TX 77843

The shrouded-impeller leakage path forces calculated by Childs (1987) have been analyzed to answer two questions. First, because of certain characteristics of the results of Childs, the forces could not be modeled with traditional approaches. Therefore, an approach has been devised to include the forces in conventional rotordynamic analyses. The forces were approximated by traditional stiffness, damping and inertia coefficients with the addition of whirl-frequency-dependent direct and cross-coupled stiffness terms. The forces were found to be well-modeled with this approach. Finally, the effect these forces had on a simple rotor-bearing system was analyzed, and, therefore, they, in addition to seal forces, were applied to a Jeffcott rotor. The traditional methods of dynamic system analysis were modified to incorporate the impeller forces and yielded results for the eigenproblem, frequency response, critical speed, transient response, and an iterative technique for finding the frequency of free vibration as well as system stability. All results lead to the conclusion that the forces have little influence on natural frequency but can have appreciable effects on system stability. Specifically, at higher values of fluid swirl at the leakage path entrance, relative stability is reduced. The only unexpected response characteristics that occurred are attributed to the nonlinearity of the model.

Introduction

The vibration of centrifugal pumps has received increasing attention recently because of the inability of current analysis techniques to adequately predict the dynamic characteristics of pump designs. Failure to accurately predict vibrations has resulted in the loss of considerable amounts of money in down time from severe vibration problems. Massey (1985), for example, described an eleven-stage pump that became unstable when its running speed exceeded its critical speed by 25 percent. In other words, it whirled at 80 percent of running speed. Another example occurred in the High Pressure Oxygen Turbopump (HPOTP) of the Space Shuttle Main Engine (SSME) which also whirled at 80 percent of running speed (Childs and Moyer, 1985).

The hydrodynamic forces generated in many of the fluid-filled gaps within the pump are well-established contributors to the problems cited above. This article is concerned specifically with the forces developed along the leakage path between the impeller and the shroud, as shown in Fig. 1. As the fluid is discharged from the impeller, some will return to the lower-pressure, suction side by way of this leakage path. Leakage is minimized typically with wear ring seals, as shown. Hydrodynamic forces are developed along the entire leakage path, i.e., the shroud section as well as the seal. Note that these are only parts of the total force on the impeller and that the impeller/volute region, balance drums, inducers, shaft, etc. also contribute to the dynamics of pumps, although they are not considered here.

Unfortunately, measurements of the total force on actual impellers have typically been obtained using pumps that have been modified to minimize leakage path forces. However, some results have been reported that are of importance here. For example, research at Cal Tech (Adkins, 1976) led to the conclusion that the pressures in the shroud annulus contributed from about 50 percent to 75 percent of the total stiffness acting on the impeller. The pump used included separation rings and an enlarged shroud clearance space to minimize leakage flow forces.

Bolleter et al. (1985) used a rocking-arm mechanism to vertically translate the spinning impeller. Their pump had normal clearances in the leakage path; and, therefore, the forces meas-

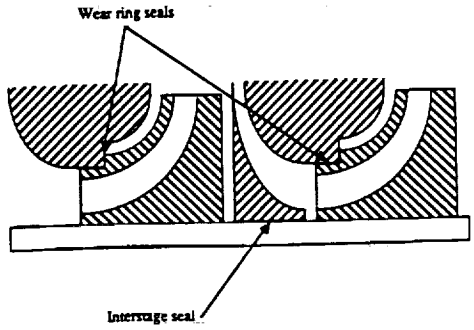

Fig. 1 Typical seal configurations for a multistage pump

Contributed by the Technical Committee on Vibration and Sound for publication in the JOURNAL OF VIBRATION AND ACOUSTICS. Manuscript received February 1990.

ured were more realistic. The results demonstrated that the nondimensionalized cross-coupled stiffness value was about twice that measured on the pump at Cal Tech (Jery et al., 1984). This suggests that the leakage path region in pumps can also reduce the stability of impeller motion. Bolleter et al. (1989) have recently presented extensive force-coefficient results at off-design conditions.

Almost all of the analytical attempts at predicting leakage path forces have been concerned with seals. However, Childs has extended his previous techniques in seal analysis (1980, 81, 82a, 82b, 82c) to apply them to the flow within the clearance space surrounding the shroud (1987). His work will be used to model the seal and shroud forces in this article and will now be summarized.

Childs used a bulk-flow approach to obtain the governing equations of the flow of a differential element of fluid. In the seal problem, three equations were required: axial- and circumferential-momentum equations as well as the continuity equation. In the shroud problem, the axial-momentum equation was replaced by a path-momentum equation, introducing additional terms which described the centrifugal and Coriolis accelerations of the fluid element. After a perturbation expansion of the equations in the eccentricity ratio, the resulting relationships were solved at various values of the whirl frequency, Ω. Integration of the resulting pressure distribution acting on the shaft or shroud yielded the radial and tangential force as functions of whirl frequency. In addition, solution was carried out at various fluid circumferential velocities at the shroud entrance. This variable is of primary importance in system stability (cross-coupled stiffness). Figure 2 shows the results of the shroud problem for three different values of the inlet swirl velocity. The leakage path analyzed corresponded to that used by Bolleter et al. (1985) which ran at 2000 rpm. Figure 3 provides the dimensions of the pump and other data of importance. The curves in Fig. 2 define force coefficients corresponding to a circular orbit of amplitude and whirl frequency ratio f. The impeller force components are linearly proportional to the orbit amplitude A. The sharp deviations

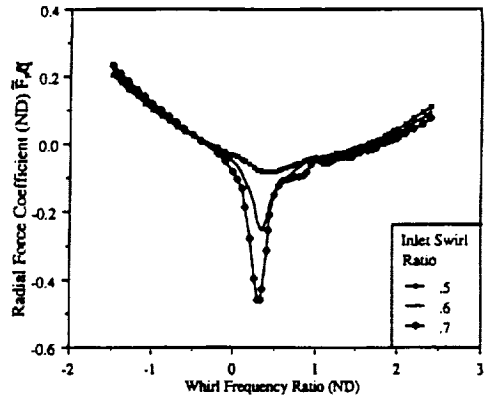

Fig. 2(*a*) Radial force coefficient curves (Childs, 1987)

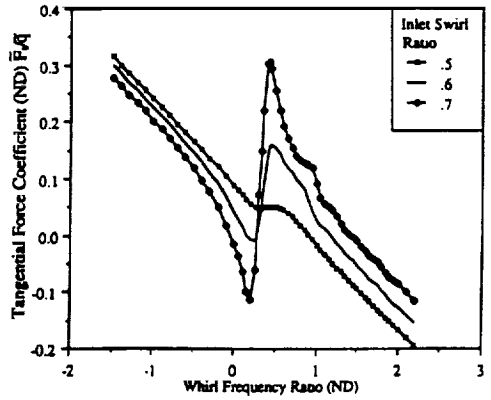

Fig. 2(*b*) Tangential force coefficient curves (Childs, 1987)

in the radial and tangential force coefficients of Fig. 2 are caused by excitation of a "centrifugal-acceleration mode" natural frequency. Childs (1990) has presented results for damped natural frequencies and eigenvalues for these modes.

Nomenclature

$\bar{C}=\frac{CQ_0\omega_s}{F_0}$ = nondimensional direct damping coefficient

$\bar{c}=\frac{cQ_0\omega_s}{F_0}$ = nondimensionalized cross-coupled damping coefficient

$\bar{F}_{r/t}=\frac{F_{r/t}}{F_0}$ = nondimensionalized radial and tangential forces on the rotor

$F_0=2R_LL\Delta P$ = (Childs, 1987)(F)

$f=\frac{\Omega}{\omega_s}$ = whirl frequency ratio

$\bar{K}=\frac{KQ_0}{F_0}$ = nondimensionalized direct stiffness coefficient

K^* = direct stiffness coefficient which is a function of the whirl frequency ratio (F/L)

$\bar{k}=\frac{kQ_0}{F_0}$ = nondimensionalized cross-coupled stiffness coefficient (Childs, 1987)

k^* = cross-coupled stiffness coefficient which is a function of the whirl frequency ratio (F/L)

L = length of seal or impeller-shroud path (L)

$\bar{M}=\frac{MQ_0\omega_s^2}{F_0}$ = nondimensionalized direct mass coefficient (Childs, 1987)

Q = rotor whirl radius (L)

Q_0 = clearance at leakage path entrance (L)

$\bar{q}=\frac{Q}{Q_0}$ = clearance ratio

R = rotor whirl amplitude (L)

$R_{L,s}$ = inlet radius of shroud leakage path or seal (L)

$\bar{u}_{tL/s}=\frac{u_{tL/s}}{R_L\omega_s}$ = nondimensionalized tangential fluid velocity at leakage path or seal entrance (inlet swirl ratio) (Childs, 1987)

x, y = rectangular coordinates of rotor center (L)

Z = complex rotor whirl amplitude (L)

$z=x+jy$ = complex rotor coordinate (L)

ϕ = phase angle of whirl from harmonic excitation

Ω = rotor whirl frequency ($1/T$)

ω_n = natural frequency of free vibration ($1/T$)

ω_s = shaft speed ($1/T$)

L = shroud leakage path coefficient subscript

r = rotor coefficient subscript

s = seal coefficient subscript

sh = shaft coefficient subscript

none = overall coefficient subscript

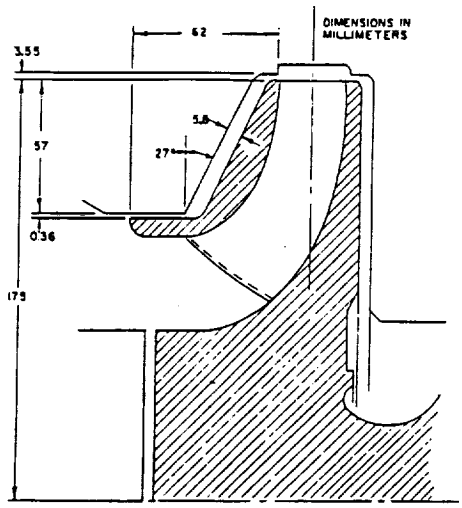

Pump data

shaft speed = ω_s = 2000 rpm

inlet clearance = Q_o = 3.55 mm

impeller exit angle = 22.5 °

flowrate = 130 l/sec

head developed = 68 m

seven-bladed impeller

working fluid is water at 80 °F

Fig. 3 Dimensions and data for the pump tested by Bolleter et al (Bolleter et al, 1985)

In the articles cited above, Childs initially suggested the following conventional, linear relationship to model the forces. It applies for small motion of the rotor about the centered position.

$$-\begin{Bmatrix} F_x \\ F_y \end{Bmatrix} = \begin{bmatrix} M & 0 \\ 0 & M \end{bmatrix} \begin{Bmatrix} \ddot{x} \\ \ddot{y} \end{Bmatrix} + \begin{bmatrix} C & c \\ -c & C \end{bmatrix} \begin{Bmatrix} \dot{x} \\ \dot{y} \end{Bmatrix} + \begin{bmatrix} K & k \\ -k & K \end{bmatrix} \begin{Bmatrix} x \\ y \end{Bmatrix}. \tag{1}$$

If circular whirl at frequency, Ω, and radius, Q, is assumed such that

$$\begin{aligned} x &= Q \cos \Omega t, \\ y &= Q \sin \Omega t, \end{aligned} \tag{2}$$

the radial and tangential force components can be stated

$$-\begin{Bmatrix} F_r \\ F_t \end{Bmatrix} = Q \begin{Bmatrix} -M\Omega^2 + c\Omega + K \\ C\Omega - k \end{Bmatrix} \tag{3}$$

After nondimensionalizing the terms as defined in Childs (1987), Eqs. (3) become

$$\begin{aligned} \frac{\bar{F}_r}{\bar{q}} &= \bar{M}f^2 - \bar{c}f - \bar{K} \\ \frac{\bar{F}_t}{\bar{q}} &= -\bar{C}f + \bar{k}, \end{aligned} \tag{4}$$

where the definitions of the coefficients are included in the Nomenclature and the other variables are defined as follows.

$\bar{F} = \dfrac{F}{2R_L L \Delta P}$, nondimensionalized force

$\bar{q} = \dfrac{Q}{Q_0}$, nondimensionalized clearance

$f = \dfrac{\Omega}{\omega}$, whirl frequency ratio

$\dfrac{\bar{F}}{\bar{q}}$, force coefficient.

The quadratic relationships of equations (4) are to be used to obtain the dynamic coefficients of equations (1). Specifically, a least-squares curve fit of the force curves will yield the coefficients. This is an adequate approach for seal forces because they, in general, do follow a quadratic trend. However, the curves of Fig. 2 illustrate that shroud forces cannot be approximated by equations (4); and, therefore, a traditional linear model as expressed in equations (1) will not adequately represent the forces. Although these results are unexpected, experimental measurements made by Franz and Arndt (1986) of impellers with inducers yielded very similar results.

Problem Definition

At this point, it is not known, assuming the force curves of Fig. 2 are valid, how they can best be included in traditional rotordynamic calculations of stability, response, critical speeds, etc. To solve this problem, the present research has been conducted to answer the following questions.

(*1*) How can the force curves found by Childs (1987) be incorporated in the traditional rotordynamic analyses of system response, stability, critical speeds, etc.?

(*2*) What effects do the forces have on a rotor-bearing system with respect to stability, natural frequencies, imbalance response, etc.?

Before answering these questions, observe that the forces present no new problems in a transient analysis because they could be applied as whirl-frequency-dependent forcing functions to a simple rotor model such as that developed by Jeffcott (1919). Although the force components are linearly proportional to the orbit amplitude, the equations of motion would be nonlinear because the forces depend on the whirl frequency, defined kinematically as

$$f = \frac{\Omega}{w_s} = \frac{x\dot{y} - y\dot{x}}{w_s(x^2 + y^2)}, \tag{5}$$

but this could be handled by integrating the equations of motion numerically with traditional methods. However, a transient analysis alone is not sufficient to obtain an understanding of the forces, and this is why answers to the questions posed above are necessary. The following section describes the model used to analyze the shroud forces, and results are then given for the eigenvalue problem and frequency response, respectively.

Rotordynamic Model

As shown in Fig. 4, the model is a Jeffcott rotor (Jeffcott, 1919) under the application of seal and shroud forces. The rotor itself represents a double-suction impeller, yielding two symmetrical leakage paths. In summary, the forces on the rotor are the shaft stiffness, two identical seal forces, and two identical shroud forces. The mathematical representation of each force will now be discussed.

A 90.7 kg (200lb) rotor is assumed. In addition, the shaft stiffness used (K_{sh} = .2987 MN/m) makes the natural frequency of forward whirl (to be defined later) equal to 80 percent of shaft speed. This choice is not completely arbitrary since this frequency corresponds to that observed in the examples cited in the Introduction (Massey, 1985; Childs and Moyer, 1985).

The seals modeled are smooth, wear ring seals with a clearance and diameter of .36 mm and 236 mm, respectively. The least-squares approach of Childs described earlier has been carried out, and the resulting dynamic coefficients are given

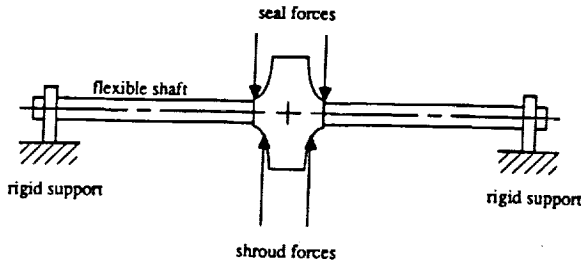

Fig. 4 Jeffcott-based, double-suction impeller leakage path model

Table 1 Coefficients for one wear ring seal

$\tilde{u}_{tL}$	M_s kg	C_s Ns/m	c_s Ns/m	K_s MN/m	k_s MN/m
.5	.3111	3356.0	78.6	.6121	.4628
.6	.3398	2167.0	89.6	.5443	.4611
.7	.3714	970.9	101.3	.4755	.4455

in Table 1. The analysis used has at times under-predicted the true value of the direct stiffness. Therefore, K_s is doubled when the coefficients of the entire model are assembled. This modification of K_s has no influence on the results, since the shaft stiffness is selected to yield a desired system natural frequency.

As described in the introduction, conventional stiffness, damping and mass coefficients cannot completely describe the impeller-shroud forces calculated by Childs and shown in Fig. 2. Therefore, the following method has been devised. First, a curve fit of the force curves is carried out, yielding dynamic coefficients which describe the quadratic variation of the forces with respect to the whirl frequency ratio as described above. The difference between these curve fits and the actual force curves is modeled by direct and cross-coupled stiffness coefficients which are functions of whirl frequency ratio. The mathematical equivalent of this approach will now be discussed.

The following modified forms of equations (4) express the method with which the impeller-shroud forces are modeled.

$$\frac{\bar{F}_r}{\bar{q}} = \bar{M}_L f^2 - \bar{c}_L f - [\bar{K}_L + \bar{K}^*(f)]$$

$$\frac{\bar{F}_t}{\bar{q}} = -\bar{C}_L f + [\bar{k}_L + \bar{k}^*(f)], \tag{6}$$

where $\bar{K}^*$ and $\bar{k}^*$ represent the nondimensionalized deviations between the force curves and the approximating quadratic expressions. Figure 5 illustrates $\bar{K}^*$ and $\bar{k}^*$, respectively. Note that, although they represent forces proportional to displacement, they are not traditional stiffness coefficients since they are functions of whirl frequency ratio. Separating the force coefficients into whirl-frequency-independent and whirl-frequency-dependent terms does not introduce any approximation to the force definitions. Equations (1) are now rewritten as

$$-\begin{Bmatrix} F_x \\ F_y \end{Bmatrix} = \begin{bmatrix} M_L & 0 \\ 0 & M_L \end{bmatrix} \begin{Bmatrix} \ddot{x} \\ \ddot{y} \end{Bmatrix} + \begin{bmatrix} C_L & c_L \\ -c_L & C_L \end{bmatrix} \begin{Bmatrix} \dot{x} \\ \dot{y} \end{Bmatrix} + \begin{bmatrix} K_L + K^*(f) & k_L + k^*(f) \\ -k_L - k^*(f) & K_L + K^*(f) \end{bmatrix} \begin{Bmatrix} x \\ y \end{Bmatrix}. \tag{7}$$

In a mathematical sense, the tangential force accounted for by k^* could be modeled as a damping coefficient; however, the result of Fig. 5(*b*) confirms the wisdom of modeling the deviation of the tangential-force coefficient by a whirl-frequency-dependent cross-coupled-stiffness-coefficient. Specifically, k^* oscillates about zero and approaches zero as the inlet swirl ratio is reduced. Finally, observe that equations (7) are,

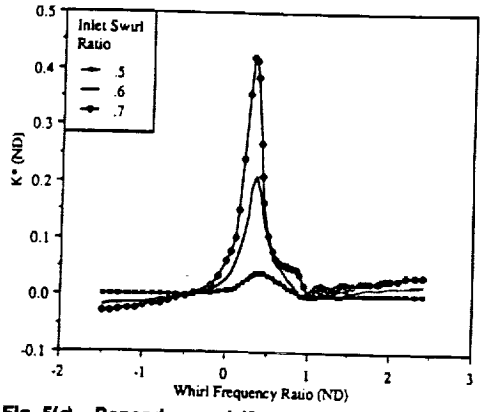

Fig. 5(*a*) Dependency of K^* on whirl frequency ratio

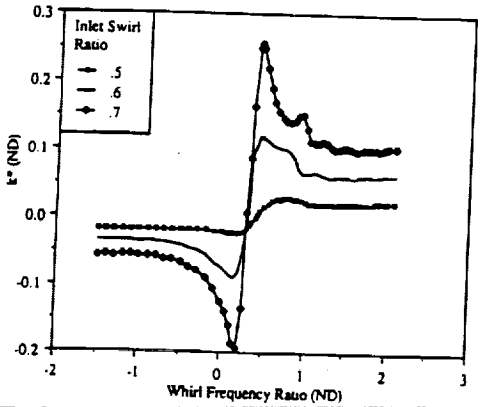

Fig. 5(*b*) Dependency of k^* on whirl frequency ratio

Table 2 Approximating coefficients for one leakage path

M_L kg	C_L Ns/m	c_L Ns/m	K_L MN/m	k_L MN/m
3.469	2037	969.9	.06781	.3137

in general, nonlinear differential equations. To understand this statement, recall that the general definition of the whirl frequency ratio, f, is given in equation (5). If the rotor precession has a constant radius and rate, f is a constant and the motion is linear. However, for general motion, f is variable and a function of the motion.

After performing the asymptotic least-squares curve fit to Fig. 2, the resulting coefficients of equation (6) are given in Table 2.

In summary, the following equations represent how the overall coefficients for the model are defined.

$$\begin{aligned} M &= M_r + 2(M_s + M_L) \\ C &= 2(C_s + C_L) + \bar{C} \\ c &= 2(c_s + c_L) \\ K &= K_{sh} + 2(2K_s + K_L) + 2K^* = \bar{K} + 2K^* \\ k &= 2(k_s + k_L) + 2k^* = \bar{k} + 2k^*. \end{aligned} \tag{8}$$

Particular coefficients are doubled because there are two seals and two leakage paths in a double suction pump. The quantity, $\bar{C}$, must be added to the model to yield reasonable stability. If the eigenvalues of the overall system are obtained without adding $\bar{C}$, the system is found to be unstable. Therefore, by adding another damping term ($\bar{C} = 10{,}422$ Ns/m), reasonable stability, which is consistent with operating pump experience, is ensured. The following equation represents the complete model used to model the forces on the rotor.

Table 3 Coefficients for overall model

$\bar{u}_{tL}$	M kg	C Ns/m	c Ns/m	K MN/m	k MN/m
.5	98.240	21208	2097.1	2.8827	1.5549
.6	98.298	18830	2119.1	2.6115	1.5494
.7	98.361	16438	2142.4	2.3363	1.5184

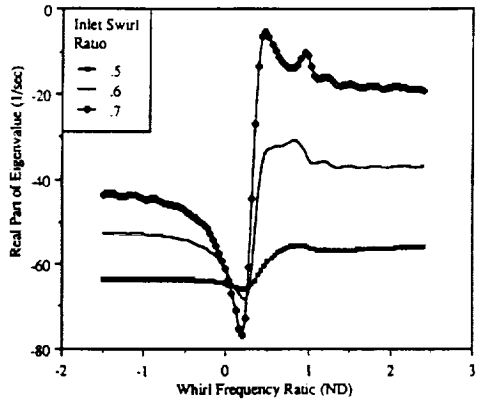

Fig. 6 Real part of the eigenvalues for the forward-whirl mode

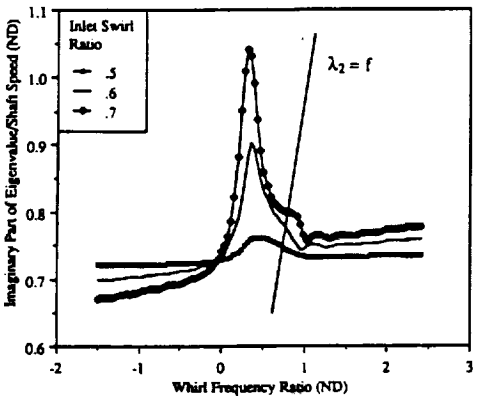

Fig. 7 Imaginary part of the eigenvalues for the forward-whirl mode

$$\begin{bmatrix} M & 0 \\ 0 & M \end{bmatrix}\begin{Bmatrix} \ddot{x} \\ \ddot{y} \end{Bmatrix} + \begin{bmatrix} C & c \\ -c & C \end{bmatrix}\begin{Bmatrix} \dot{x} \\ \dot{y} \end{Bmatrix} + \begin{bmatrix} K(f) & k(f) \\ -k(f) & K(f) \end{bmatrix}\begin{Bmatrix} x \\ y \end{Bmatrix} = \begin{Bmatrix} F_x \\ F_y \end{Bmatrix}. \quad (9)$$

Table 3 contains the numerical values for this analysis. These coefficients combine to make the damping for the uncoupled system, defined by $C/2\sqrt{KM}$, equal to 63 percent, 59 percent, and 54 percent of critical damping for the three swirl ratios shown, respectively. Again, $\bar{K}^*$ and $\bar{k}^*$ are illustrated in Fig. 5 and are defined analytically with cubic-spline curve fits.

Natural Frequency Determination

The characteristic equation for Eq. (9) is

$$[M\bar{s}^2 + C\bar{s} + K(f)]^2 + [c\bar{s} + k(f)]^2 = 0, \quad (10a)$$

where $\bar{s} = s/\omega_s$. For each whirl-frequency ratio f, two pairs of complex conjugate roots of the form

$$\bar{s} = \sigma_i \pm j\lambda_i; \quad i = 1,2 \quad (10b)$$

can be calculated corresponding to forward and backward whirling modes. The concern here is finding the natural frequency for forward whirling motion. Figure 7 illustrates the eigenvalue solutions to Eq. (10a) versus f.

Table 4 Natural frequencies of free vibration for the pump model with and without K^* and k^*

$\bar{u}_{tL}$	$\frac{\omega_n}{\omega_s}$ with K^* and k^*	$\frac{\omega_n}{\omega_s}$ without K^* and k^*	Percent Decrease
.5	.747	.727	2.68%
.6	.777	.724	6.82%
.7	.800	.715	10.63%

Table 5 Real parts of the eigenvalues for the model with and without K^* and k^*

$\bar{u}_{tL}$	Real part with K^* and k^* $1/sec$	Real part without K^* and k^* $1/sec$	Percent Decrease
.5	-55.9	-60.3	7.87%
.6	-31.1	-47.2	51.80%
.7	-13.8	-34.5	150.00%

Free whirl of the rotor occurs only when the imaginary part of an eigenvalue equals the whirl frequency ratio f in Fig. 7; i.e., $\lambda_2 = f$. The three points at which the $\lambda_2 = f$ line intersects the $\lambda(f)$ curves defines the forward-whirl natural frequencies for the three inlet swirl ratios. The real part of the eigenvalue at this natural frequency defines the rotor's damping.

To find the "natural frequency" and damping of free whirl, the following iterative technique has been used. First, a whirl frequency ratio is assumed. From this value, the corresponding values of K and k are obtained from the data shown in Fig. 5 from which the eigenvalues are found using Eq. (10). These first two steps are equivalent to finding a point on the curves of Figs. 6 and 7. The imaginary part of the forward-whirl eigenvalue is compared to the whirl frequency used. If they are the same, the natural frequency at which free vibration takes place is defined. If they are different, the imaginary part of the forward-whirl root becomes the assumed whirl frequency ratio, and the same steps are carried out until convergence occurs. Note that this calculation procedure yields the damped natural frequency for the system.

Tables 4 and 5 show results of the above algorithm. Also included are the eigenvalues of the same model neglecting K^* and k^*, which correspond to a pure quadratic approximation of the leakage path forces as in equations (4). The eigenvalues illustrate at least two important conclusions about the effects of the values of K^* and k^*. First, the natural frequency increases when K^* and k^* are included as well as when the swirl ratio is increased. The variation of K^* in Fig. 5 explains these observations. More importantly, the percent differences between the two models show that the values of K^* and k^* have very little effect on natural frequency. Second, stability is reduced when K^* and k^* are included and when the swirl ratio is increased. The variation of k^* in Fig. 5 is the cause of these observations. Finally, the percent differences between the two models shows that K^* and k^* can cause appreciable reductions in relative stability.

To show that the stability and frequency of free vibration are determined only by the root obtained from the iterative approach described earlier, the equations of motion (9) were integrated in a series of transient, free-vibration simulations. Initial conditions were an initial displacement of .127 mm (.005 in) and velocity equal to $R_L w_s$ (synchronous whirl). Figure 8 includes the resulting orbit and a time history of the whirl frequency ratio for free vibration and an inlet swirl ratio of 0.7. As shown, the rotor executed a well-damped spiral orbit.

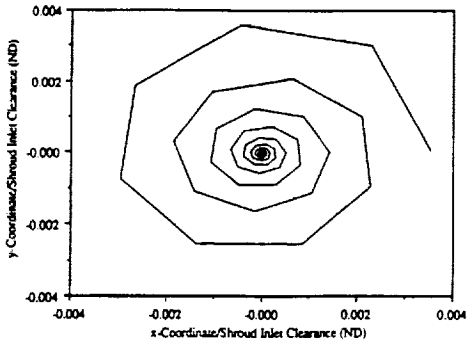

Fig. 8(*a*) Rotor orbit during free vibration

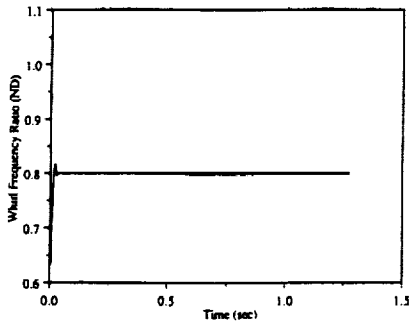

Fig. 8(*b*) Time history of rotor whirl frequency ratio during free vibration

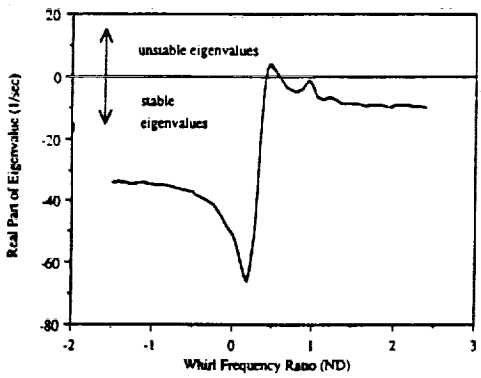

Fig. 9 Real part of the eigenvalues for the forward-whirl mode with a 12.5 percent reduction in direct damping

The whirl frequency ratio of the orbit was exactly 0.8, which corresponds to the natural frequency found earlier. The other two swirl ratios yield similar results.

To verify that the stability of the model is described only by the real part of the eigenvalues obtained with the iterative approach described above, the direct damping coefficient was reduced by 12.5 percent producing a range of unstable eigenvalues as shown in Fig. 9 where the real part of the forward-whirl root is positive between whirl frequency ratios of 0.41 and 0.57. The natural frequency of this altered model corresponds to a stable eigenvalue and is $.825w_s$. Integration of the equations of motion were altered to include a harmonic forcing function with an amplitude of 5N which forced the rotor in a circular direction at a frequency of $.5w_s$. Figure 10 includes the resulting orbit, whirl frequency ratio time history, and a Fast Fourier Transform (FFT) of the x-coordinate, respectively. Even though the forcing frequency was within the unstable range of frequencies, the figures show that the system was stable in that its orbit did not grow without bound. The loops and limit cycle behavior are the results of the nonlinearities in the model. The FFT shows that the steady state orbit consisted of response at both the forcing frequency, $.5w_s$, and the natural frequency, $.825w_s$. Other forcing frequencies were

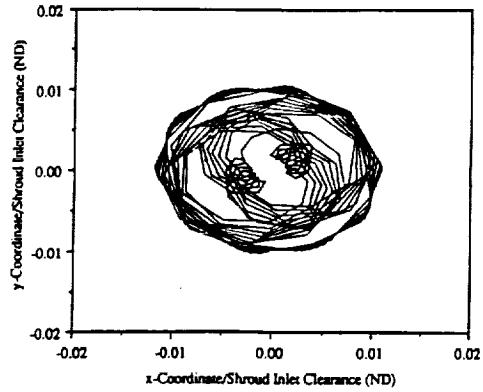

Fig. 10(*a*) Rotor orbit during harmonic excitation at 50 percent of shaft speed and 12.5 percent reduction in direct damping

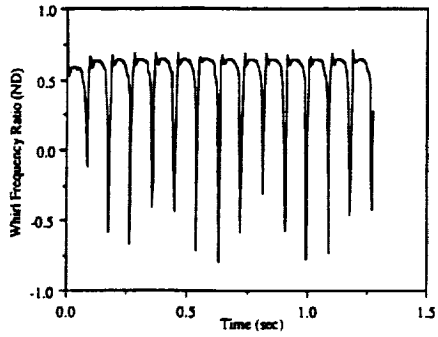

Fig. 10(*b*) Time history of rotor whirl frequency ratio during harmonic excitation at 50 percent of shaft speed and a 12.5 percent reduction in direct damping

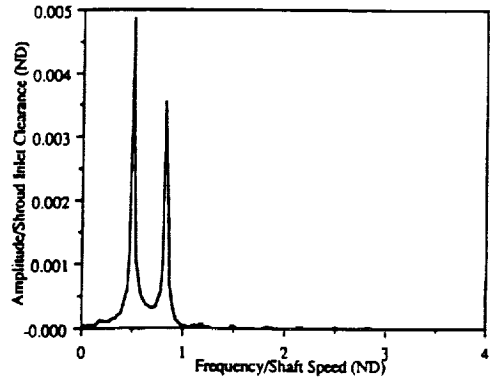

Fig. 10(*c*) FFT of the response of the rotor during harmonic excitation at 50 percent of shaft speed and a 12.5 percent reduction in direct damping

also tried. Using a stable value of $0.7w_s$, for example, the response did not behave in the same manner; instead, the orbit reached a steady state circular path at the excitation frequency as would be expected from a linear system. However, forcing at $.375w_s$, the characteristics of the results from forcing at $.5w_s$ occurred again, as can be seen in Fig. 11, which again contain the orbit, time history of the whirl frequency ratio and an FFT of the response. Only forcing frequencies below and within the unstable zone resulted in this behavior. Only when the direct damping coefficient was reduced until the natural frequency corresponded to an unstable eigenvalue did the response become unstable in a linear sense, where the orbit grew without bound at the natural frequency. The fundamental result from this analysis is a verification that a range of whirl frequencies yielding eigenvalues with positive real parts does not cause the system response to grow without bound unless it includes the system natural frequency. In addition, the non-

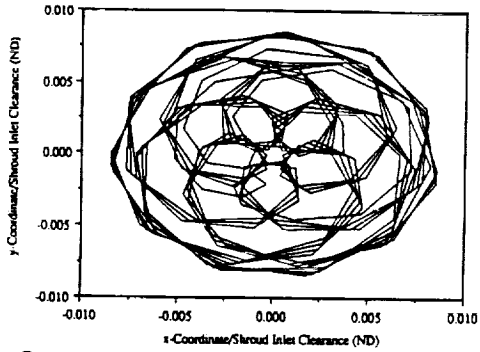

Fig. 11(a) Rotor orbit during harmonic excitation at 37.5 percent of shaft speed and a 12.5 percent reduction in direct damping

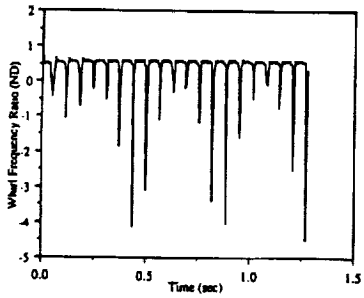

Fig. 11(b) Time history of rotor whirl frequency ratio during harmonic excitation at 37.5 percent of shaft speed and a 12.5 percent reduction in direct damping

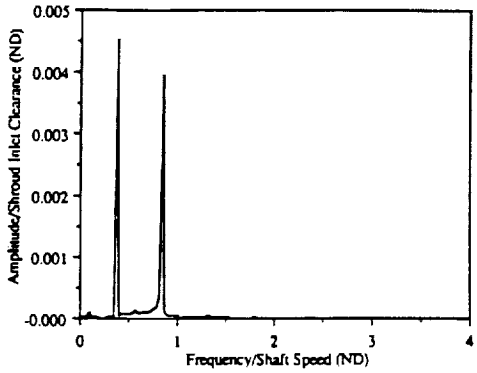

Fig. 11(c) FFT of the response of the rotor during harmonic excitation at 37.5 percent of shaft speed and a 12.5 percent reduction in direct damping

linearities of the system can cause a limit cycle to occur under certain conditions.

Finally, the critical speed of the rotor cannot be calculated unless force curves are available at other shaft speeds. In this case, the natural frequency is calculated with the iterative method just described, but at a number of shaft speeds. A plot of natural frequency as a function of shaft speed is then drawn, analogous to "critical speed maps" in fluid-film bearing analysis. The critical speed is defined as the speed where the natural frequency is equal to the shaft speed.

Frequency Response

As discussed earlier, the following are the equations of motion of the model

$$\begin{bmatrix} M & 0 \\ 0 & M \end{bmatrix}\begin{Bmatrix} \ddot{x} \\ \ddot{y} \end{Bmatrix} + \begin{bmatrix} C & c \\ -c & C \end{bmatrix}\begin{Bmatrix} \dot{x} \\ \dot{y} \end{Bmatrix} + \begin{bmatrix} K(f) & k(f) \\ -k(f) & K(f) \end{bmatrix}\begin{Bmatrix} x \\ y \end{Bmatrix} = F\begin{Bmatrix} \cos\Omega t \\ \sin\Omega t \end{Bmatrix}, \quad (11)$$

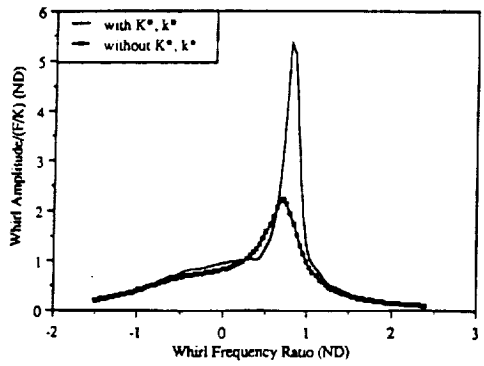

Fig. 12 Frequency response: whirl amplitude

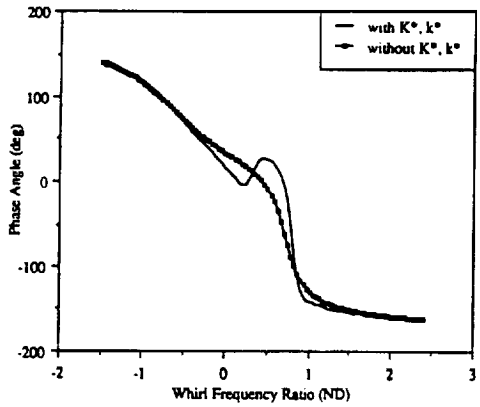

Fig. 13 Frequency response: phase angle

where the right-hand side represents a harmonic forcing function appropriate to frequency response analyses. As in traditional methods, the transient solution is assumed to decay with time, and only the steady-state response of the rotor is considered. Obviously, frequency response solutions are only valid when the system is stable, precluding the type of response illustrated in Figs. 10 and 11. The forcing frequency is defined by Ω which has been used to represent whirl speed. Since the steady-state motion is assumed to occur at the same frequency as the excitation, this should not cause confusion. Note that the model is now linear because the whirl frequency ratio and, hence, the stiffnesses are constant. Multiplying the second equation by the complex number i, the equations can be combined into one in terms of the complex variable z.

$$M\ddot{z} + (C - ic)\dot{z} + (K - ik)z = Fe^{j\Omega t}. \quad (12)$$

Assuming steady-state motion of the following form

$$z = Re^{j\phi}, \quad (13)$$

where R denotes the whirl amplitude, and ϕ is the phase angle yields

$$\frac{R}{F/K} = \frac{K}{\sqrt{[K - M\Omega^2 + c\Omega]^2 + [C\Omega - k]^2}}$$
$$\phi = \tan^{-1}\left[\frac{k - C\Omega}{K - M\Omega^2 + c\Omega}\right]. \quad (14)$$

Equations (14) were solved using the present model data, and the results for a swirl ratio of 0.7 are shown in Figs. 12 and 13. Also included are the same results for the model with K^* and k^* neglected. Again, in obtaining frequency curves as shown in Figs. 12 and 13, the stiffness terms must be calculated at the corresponding whirl frequency ratio.

The swirl ratio of 0.7, used in Figs. 12 and 13, exhibited the largest variation in amplitude and phase at the whirl frequency ratio of .80, the system natural frequency. An amplitude dif-

ference of about 60 percent is shown between the curves, suggesting that K^* and k^* have significant influence on the system primarily at this frequency. The swirl ratios of 0.6 and 0.5 exhibited similar but decreasing results in both the amplitude and phase curves, having differences in amplitude at the peak value of 35 percent and 6 percent, respectively. In fact, the curves were almost identical in the case corresponding to a swirl ratio of 0.5. Note that these resonance peaks occurred in all cases at the corresponding natural frequencies found in the previous section, further verifying the preceding results. The difference in the response to synchronous imbalance excitation ($f = 1$) between the two models is small, and this suggests that the leakage path forces have negligible effects on imbalance response. However, the presence of a subsynchronous excitation near the natural frequency can result in large increases in response amplitude when k^* is included.

Summary and Conclusions

The impeller-shroud forces have been separated into (*a*) constant (whirl frequency-independent) stiffness, damping and mass coefficients and (*b*) direct and cross-coupled added stiffness coefficients which are functions of whirl frequency. With this approach, the model can be analyzed using traditional techniques with a few modifications. A new iterative technique was used in the determination of the rotor's natural frequency and damping. The whirl-frequency-dependent stiffness terms were seen to be convenient and effective models for the impeller-shroud force nonlinearities.

When the values of the added stiffness coefficients, K^* and k^*, were included in addition to the frequency-independent coefficients, a number of effects resulted. First, the natural frequency was seen to increase by a small amount, suggesting that K^* could be neglected when only the natural frequency is important. In addition, the stability is seen to decrease when k^* is included. This effect is appreciable, so stability calculations should include k^*. The frequency response analysis showed synchronous response to imbalance is increased by the stiffnesses although by only a small amount. Appreciable differences in response due to subsynchronous excitation occur only at or near the natural frequency and become negligible at low values of the inlet swirl ratio.

The nonlinearity introduced by the whirl-frequency-dependency of the force coefficients resulted in limit cycles and nonsynchronous response in some cases.

References

Adtkins, D., 1976, "Analyses of Hydrodynamic Forces on Centrifugal Pump Impellers," M.S. Thesis, California Institute of Technology, Pasadena.

Bolleter, U., Wyss, A., Welte, I., and Sturchler, R., 1985, "Measurements of Hydrodynamic Interaction Matrices of Boiler Feed Pump Impellers," ASME, Paper No. 85-DET-148.

Bolleter, U., Leibundgut, E., Sturchler, R., and McCloskey, T., 1989, "Hydraulic Interaction and Excitation Forces of High Head Pump Impellers," presented at the ASCE/ASME Pumping Machinery Symposium, July 9-12, 1989.

Childs, D., Dressman, J., and Childs, S., 1980, "Testing of Turbulent Seals for Rotordynamic Coefficients," *Proc. of Workshop on Rotordynamic Instability Problems in High Performance Turbomachinery*, Texas A&M University, NASA CP-2133, pp. 121-38.

Childs, D., 1981, "Convergent-Tapered Annular Seals: Analysis for Rotordynamic Coefficients," Symposium Vol., Fluid/Structure Interactions Turbomach., ASMW Winter Annual Meeting, pp. 35-44.

Childs, D., 1982a, "Dynamic Analysis of Turbulent Annular Seals Based on Hirs' Lubrication Equations," ASME Paper No. 82-Lub-41.

Childs, D., 1982b, "Finite-Length Solutions for Rotordynamic Coefficients of Turbulent Annular Seals," ASME Paper No. 82-Lub-42.

Childs, D., and Dressman, J., 1982c, "Testing of Turbulent Seals for Rotordynamic Coefficients," *Proceedings of Workshop on Rotordynamic Instability Problems in High Performance Turbomachinery*, Texas A&M University, NASA CP-2250, pp. 157-71.

Childs, D., and Moyer, D., 1985, "Vibration Characteristics of the HPOTP (High Pressure Oxygen Turbopump) of the SSME (Space Shuttle Main Engine)," ASME *Journal of Engineering for Gas Turbines and Power*, Vol. 107, pp. 152-159.

Childs, D., 1987, "Fluid-Structure Interaction Forces At Pump-Impeller-Shroud Surfaces for Rotordynamic Calculations," Texas A&M University, Mechanical Engineering Dept., ASME Vibration Conference, Boston, Mass.

Childs, D., 1990, "Centrifugal-Acceleration Modes for Incompressible Fluid in the Leakage Analysis Between a Shrouded Pump Impeller and Its Housing," ASME JOURNAL OF VIBRATION AND ACOUSTICS, May 1990.

Franz, R., and Arndt, N., 1986, "Measurement of Hydrodynamic Forces on the Impeller of the SSME," Report No. E249.2, California Institute of Technology, Pasadena.

Jeffcott, H., 1919, "The Lateral Vibration of Loaded Shafts in the Neighborhood of a Whirling Speed—The Effect of Want of Balance," The Philosophical Magazine, Vol. 6, No. 37, pp. 304-314.

Jery, B., Acosta, J., Brennen, C., and Caughey, T., 1984, "Hydrodynamic Impeller Stiffness, Damping and Inertia In the Rotordynamics of Centrifugal Flow Pumps," *Proceedings of Workshop on Rotordynamic Instability Problems in High Performance Turbomachinery*, Texas A&M University, NASA CP-2338, pp. 137-160.

Massey, I. C., 1985, "Subsynchronous Vibration Problems in High Speed Multistage Centrifugal Pumps," *Proceedings of the 14th Turbomachinery Symposium*, Turbomachinery Laboratories, Texas A&M University, pp. 11-16.

Childs, D.
(1992b)

Reprinted from March 1992, Vol. 114, Journal of Fluids Engineering

Pressure Oscillation in the Leakage Annulus Between a Shrouded Impeller and Its Housing Due to Impeller-Discharge-Pressure Disturbances

D. W. Childs
Turbomachinery Laboratories,
Mechanical Engineering Department,
Texas A&M University,
College Station, Texas 77843

An analysis is presented for the perturbed flow in the leakage path between a shrouded-pump impeller and its housing caused by oscillations in the impeller-discharge pressure. A bulk-flow model is used for the analysis consisting of the path-momentum, circumferential-momentum, and continuing equations. Shear stress at the impeller and housing surfaces are modeled according to Hirs' turbulent lubrication model. In the present analysis, perturbations of the impeller discharge pressure are used to excite the fluid annulus. The circumferential variation of the discharge pressure is expanded in a Fourier series up to order n_1, where n_1 is the number of impeller blades. A precession of the impeller wave pattern in the same direction or opposite to pump rotation is then assumed to completely define the disturbance excitation. Predictions show that the first (lowest-frequency) "centrifugal-acceleration" mode of the fluid within the annulus has its peak pressure amplitude near the wearing-ring seal. Pressure oscillations from the impeller can either be attenuated or (sharply) magnified depending on: (a) the tangential velocity ratio of the fluid entering the seal, (b) the order of the fourier coefficient, and (c) the closeness of the precessional frequency of the rotating pressure field to the first natural frequency of the fluid annulus, and (d) the clearance in the wearing-ring seal.

Introduction

The present work is stimulated by experiences with the SSME HPFTP (Space Shuttle Main Engine, High Pressure Fuel Turbopump) wearing-ring seals. A stepped, 3-cavity, tooth-on-rotor, labyrinth-seal design is used. The stator for the seal is made from KEL-F, a plastic that is somewhat similar to nylon. In some cases, post-test inspection of the stator element has revealed that interior points in the stator material have melted and then resolidified, despite being in contact with liquid hydrogen. One hypothesis for this exceptional outcome was that the material had been subjected to cyclical stresses which generated heat due to hysteresis. Because of poor conduction properties of the material, the heat could not be dissipated, the temperature rose, and melting resulted. "What pressure oscillations are driving the cyclical stresses?", is an obvious question in reviewing this scenario. The present analysis examines "centrifugal-acceleration" modes, arising between the impeller shroud and its housing and driven by pressure oscillations from the pump, as an answer to this question.

Figure 1 illustrates an impeller stage of a multi-stage centrifugal pump. Leakage along the front side of the impeller, from impeller discharge to inlet, is restricted by a wearing-ring seal, while leakage along the back side is restricted by either an interstage seal or a balance-piston discharge seal. The present analysis considers perturbed flow in the leakage paths between the impeller-shroud surface and its housing.

Prior analyses by the author of those annulli have been concerned with lateral (1987, 1989) and axial (1990a) reaction forces developed by the impeller shrouds as a consequence of harmonic clearance changes due to impeller motion. These analyses have been based on "bulk-flow" models which neglect the variation in the dependent variables across the fluid film. The model consists of the path and circumferential momentum equations and the continuity equations.

The analyses cited have yielded force and moment coefficients due to impeller motion but have also predicted "resonance" phenomena, which are caused by the centrifugal-acceleration body forces present in the path momentum equations. An algorithm was developed (1990b) to calculate the complex eigenvalues and eigenvectors associated with these resonances. In the present analysis, the harmonic response of the flow within the annulus is examined due to time and circumferential variations in the discharge pressure of the impeller.

[1]The work reported herein was supported by NASA Marshall Space Flight Center under contract NAS 8-37821; contract technical monitor: James Cannon.
Contributed by the Fluids Engineering Division for publication in the JOURNAL OF FLUIDS ENGINEERING. Manuscript received by the Fluids Engineering Division August 20, 1990.

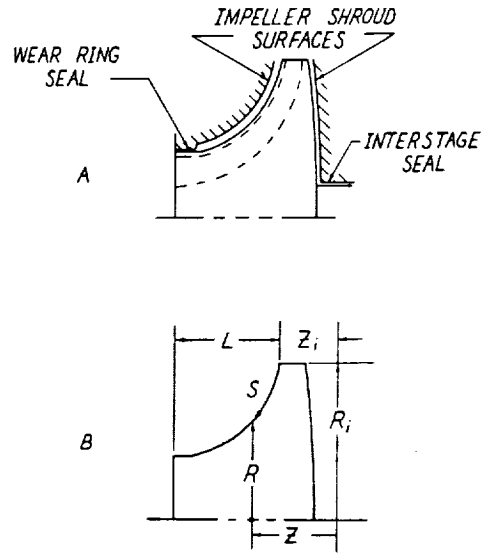

Fig. 1 Impeller leakage paths

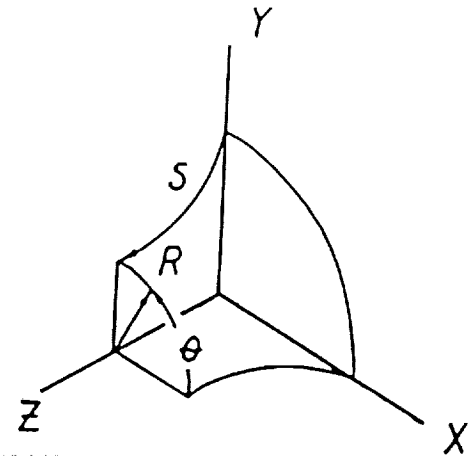

Fig. 2 Impeller surface geometry

Geometry and Kinematics

Figure 1 illustrates the annular leakage paths along the front and back sides of a typical shrouded impeller of a multistage centrifugal pump. The present discussion concentrates on the flow and pressure fields within the forward annulus; however, the analysis can also be applied to the rear annulus.[2] As illustrated in Fig. 2, the outer surface of the impeller is a surface of revolution formed by rotating the curve $R = R(Z)$ about the Z axis. A point on the surface may be located by the coordinates $Z, R(Z), \theta$. The length along the curve $R(Z)$ from the initial point R_i, Z_i to an arbitrary point R, Z is denoted by S and defined by

$$S = \int_{Z_i}^{Z} \sqrt{1 + \left(\frac{dR}{dZ}\right)^2}\, du = \int_{R_i}^{R} \sqrt{1 + \left(\frac{dZ}{dR}\right)^2}\, du \qquad (1)$$

In the equations which follow, the path coordinate S and angular coordinate θ are used as independent spatial variables. The coordinates Z, R defining the impeller surface are expressed as parametric functions of S, i.e., $Z(S)$, $R(S)$. The length of the leakage path along the impeller face is defined by

$$L_s = \int_{Z_i}^{Z_i + L} \sqrt{1 + \left(\frac{dR}{dZ}\right)^2}\, du \qquad (2)$$

Governing Equations

Returning to Fig. 2, the path coordinate S and circumferential coordinate $R\theta$ are used to locate a fluid differential

[2]Although the leakage flow is normally up the backside of all impellers except the last impeller, the governing equations would continue to be valid irrespective of the flow direction.

Nomenclature

$A_{2s}, A_{3s}, A_{2\theta}, A_{3\theta}$ = coefficients introduced in Eq. (12)
$b = V_i/R\omega$ = nondimensional velocity ratio
C_{de} = discharge coefficient for the exit wearing seal introduced in Eq. (7)
C_i = initial ($s = 0$) clearance (L)
C_r = exit seal clearance (L)
$f = \Omega/\omega$ = nondimensional precession frequency
f^* = nondimensionalized precession frequency yielding a maximum response pressure
$f^{+1} = \dfrac{n_1}{(n_1 - n_2)}$ = positive, dominant, nondimensional, precession frequency predicted for an impeller with n_1 blades in a diffuser with n_2 blades
$h = H/C_i$ = nondimensionalized clearance
H = clearance between impeller shroud and housing (L)
L_s = leakage-path length, defined by Eq. (2), (L)
n = order of Fourier coefficient, introduced in Eq. (13).
$p = P/\rho V_i^2$ = nondimensional static fluid pressure
$p_s(\theta,t)$ = prescribed annulus supply pressure (impeller exit pressure)
$p_e(\theta,t)$ = prescribed annulus exit pressure (impeller inlet pressure)
P = fluid static pressure (F/L^2)
R = radial coordinate (L)
R_i = initial ($s = 0$) radius (L)
$r = R/R_i$ = nondimensionalized radial coordinate
$R_s = 2HU_s/\nu$ = path-velocity Reynolds number
S = path coordinate introduced in Eq. (1), (L)
$s = S/L_s$ = nondimensionalized path length
$T = L_s/V_i$ = representative transit time for fluid traversing the leakage path (T)
$u_s = U_s/V_i$ = nondimensionalized path fluid velocity
$u_\theta = U_\theta/R_i\omega$ = nondimensionalized circumferential fluid velocity
V_i = initial ($s = 0$) path fluid velocity
ϵ = perturbation coefficient
ω = pump running speed (T^{-1})
Ω = excitation frequency (T^{-1})
ρ = fluid density (M/L^3)
θ = circumferential coordinate
σ_r, σ_s = normalized friction factors, defined by Eq. (11)
$\tau = \tau t$ = nondimensionalized time
ξ = entrance-loss coefficient introduced in Eq. (7)
ν = kinematic viscosity (L^2T^{-1})

Overbars denote complex variables; see Eq. (16). Subscripts 0 and 1 denote zeroth- and first-order solutions, respectively.

element of thickness $H(S, \theta, t)$. From Childs (1987), the continuity equation can be stated

$$\frac{\partial H}{\partial t}+\frac{\partial}{\partial S}(U_s H)+\frac{1}{R}\frac{\partial}{\partial \theta}(U_\theta H)+\left(\frac{H}{R}\right)\frac{\partial R}{\partial S}U_s=0 \quad (3a)$$

where U_s and U_θ are the path and circumferential bulk-velocity components, respectively. The path and circumferential momentum equations are stated

$$-H\frac{\partial P}{\partial S}=\tau_{ss}+\tau_{sr}-\rho H\frac{U_\theta^2}{R}\frac{dR}{dS}+\rho H\left(\frac{\partial U_s}{\partial t}+\frac{\partial U_s}{\partial \theta}\frac{U_\theta}{R}+\frac{\partial U_s}{\partial S}U_s\right) \quad (3b)$$

$$-\frac{H}{R}\frac{\partial P}{\partial \theta}=\tau_{\theta s}+\tau_{\theta r}+\rho H\left(\frac{\partial U_\theta}{\partial t}+\frac{\partial U_\theta}{\partial \theta}\frac{U_\theta}{R}+\frac{\partial U_\theta}{\partial S}U_s+\frac{U_\theta U_s}{R}\frac{\partial R}{\partial S}\right) \quad (3c)$$

Following Hirs' approach (1973), the wall shear-stress definitions in these equations can be stated

$$\tau_{ss}=\frac{ns}{2}\rho U_s^2 R_s^{ms}[1+(U_\theta/U_s)^2]^{\frac{ms+1}{2}}$$

$$\tau_{sr}=\frac{nr}{2}\rho U_s^2 R_s^{mr}\{1+[(U_\theta-R\omega)/U_s]^2\}^{\frac{mr+1}{2}}$$

$$\tau_{\theta s}=\frac{ns}{2}\rho U_\theta U_s R_s^{ms}[1+(U_\theta/U_s)^2]^{\frac{ms+1}{2}}$$

$$\tau_{\theta r}=\frac{nr}{2}\rho U_s(U_\theta-R\omega)R_s^{mr}\{1+[(U_\theta-R\omega)/U_s]^2\}^{\frac{mr+1}{2}} \quad (4)$$

where

$$R_s=2HU_s/\nu \quad (5)$$

Nondimensionalization and Perturbation Analysis

The governing equations define the bulk-flow velocity components (U_s, U_θ) and the pressure P as a function of the coordinates ($R\theta$, S) and time, t. They are conveniently nondimensionalized by introducing the following variables

$$u_s=U_s/V_i, \quad u_\theta=U_\theta/R_i\omega, \quad p=P/\rho V_i^2$$

$$s=S/L_s, \quad r=R/R_i, \quad b=V_i/R_i\omega$$

$$\tau=\omega t, \quad T=L_s/V_i \quad (6)$$

The present analysis examines the changes in (u_s, u_θ, p) due to changes in the impeller's discharge or inlet pressure. Following conventional notation, pressure drops at the annulus inlet and exit are stated

$$P_s(\theta,t)-P(0,\theta,t)=\rho(1+\xi)U_s^2(0,\theta,t)/2$$

$$P(L_s,\theta,t)-P_e(\theta,t)=\rho C_{de}U_s^2(L_s,\theta,t)/2 \quad (7)$$

Note specifically that the (upstream) supply and (downstream) exit pressure are now functions of time. Assume that the oscillations consist of a small perturbation of the form

$$P_s(\theta,t)=P_{s0}+\epsilon P_{s1}(\theta,t), P_e(\theta,t)=P_{e0}+\epsilon P_{e1}(\theta,t)$$

and introduce nondimensional variables to yield the following zeroth

$$p_0(0)=p_{s0}-(1-\xi)/2$$

$$p(1)=p_{es}+C_{de}u_{s0}^2(1)/2 \quad (8)$$

and first-order equations

$$p_{s1}(\theta,t)-p_1(0,\theta,t)=(1+\xi)u_{s1}(0,\theta,t)$$

$$p_1(1,\theta,t)-p_{e1}(\theta,t)=C_{de}u_{s0}(1)u_{s1}(1,\theta,t) \quad (9)$$

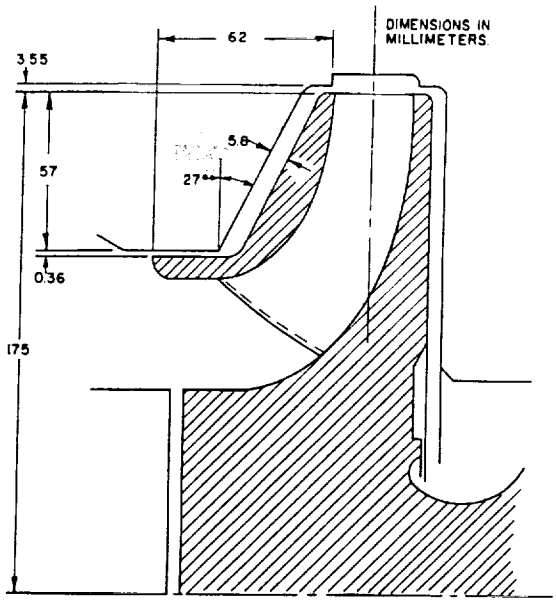

Fig. 3 Example impeller; Bolleter et al. (1987)

The perturbed supply and exit pressures $p_{s1}(\theta,t)$, $p_{e1}(\theta,t)$ can now be specified functions of time and provide excitation for the perturbed flowfield within the annulus.

Expansion of the dependent variables of Eq. (3) in perturbation equations yields:

Zeroth-Order Equations

(a) Path-Momentum Equation

$$\frac{dp_o}{ds}-\frac{1}{r}\left(\frac{dr}{ds}\right)\frac{u_{\theta o}^2}{b^2}+\left[\left(\frac{\sigma_r+\sigma_s}{2}\right)-\frac{1}{h_o}\frac{dh_o}{ds}-\frac{1}{r}\frac{dr}{ds}\right]u_{so}^2=0 \quad (10a)$$

(b) Circumferential-Momentum Equation

$$\frac{du_{\theta o}}{ds}+\frac{u_{\theta o}}{r}\frac{dr}{ds}+[\sigma_r(u_{\theta o}-r)+\sigma_s u_{\theta o}]/2=0 \quad (10b)$$

(c) Continuity Equation

$$rh_o u_{so}=1 \quad (10c)$$

The quantities σ_s and σ_r are defined by

$$\sigma_s=(L_s/H_o)\lambda_s, \quad \sigma_r=(L_s/H_o)\lambda_r \quad (11)$$

where λ_s and λ_r are the dimensionless stator and rotor friction factors:

$$\lambda_s=nsR_{so}^{ms}[1+(u_{\theta o}/bu_{so})^2]^{\frac{ms+1}{2}}$$

$$\lambda_r=nrR_{so}^{mr}\{1+[(u_{\theta o}-r)/bu_{so}]^2\}^{\frac{mr+1}{2}}$$

The continuity equation has been used to eliminate du_{so}/ds from Eq. (10a). The momentum equations define the pressure and velocity distributions for a centered impeller position. They are coupled and nonlinear and must be solved iteratively. The initial condition for $u_{\theta o}(0)$ is obtained from the exit flow condition of the impeller. Zeroth-order pressure boundary conditions are provided by Eq. (8).

Figure 3 illustrates the pump-impeller and shroud geometry used by Bolleter et al. (1987) in their test program for radial force coefficients. Their tests were at best efficiency point (BEP) with the pump running at 2000 rpm, while developing 68m of head and 130l/s of flow rate. The impeller has seven blades and an impeller exit angle of 22.5°. The test fluid is water at 26.6°C. For the present study, ΔP across the impeller is assumed to be 70 percent of the total head rise of the stage. Based on pitot-tube measurements, impeller-exit-tangential velocity is about 50 percent of the impeller discharge surface velocity; hence, $u_{\theta 0} \cong 0.5$.

Table 1 Zeroth-order-solution results; C_i = 3.5mm, C_r = 0.36mm

$u_{\theta o}(0)$	0.5	0.6	0.7
R_{so}	9377	8907	8426
C_{de}	2.068	2.098	2.130
$\dot{m}$ (kg/sec)	4.448	4.225	3.997

Table 1 provides the zeroth-order solutions for new (original-clearance) exit wearing-ring seals. The R_{so} values on the order of 10,000 are low in comparison to the circumferential Reynolds number $R_{\theta 0} = 2HU_{\theta 0}/\nu$ which varies along the path, but is on the order of 250,000. These leakage results were obtained iteratively starting with guessed values for the seal inlet values of pressure and tangential velocities and yielding an initial estimate for C_{de}. With this estimate for C_{de}, the leakage is calculated through the annulus which yields new inlet conditions for the seal. Solutions are "bounced" back and forth between the seal and the annulus until the same leakage value is obtained for both flow paths (four-place accuracy).

First-Order Equations

(a) Path-Momentum Equation

$$\frac{\partial p_1}{\partial s} + u_{\theta 1}A_{2s} + u_{s1}A_{3s} + \left[\omega T \frac{\partial u_{s1}}{\partial \tau} + \omega T \frac{u_{\theta o}}{r}\frac{\partial u_{s1}}{\partial \theta} + u_{so}\frac{\partial us_1}{\partial s}\right] = 0 \quad (12a)$$

(b) Circumferential-Momentum Equation

$$b\frac{L_s}{R_i}\frac{1}{r}\frac{\partial p_1}{\partial \theta} + u_{\theta 1}A_{2\theta} + u_{s1}A_{3\theta} + \left[\omega T \frac{\partial u_{\theta 1}}{\partial \tau} + \omega T \frac{u_{\theta o}}{r}\frac{\partial u_{\theta o}}{\partial \theta} + u_{so}\frac{\partial u_{\theta 1}}{\partial s}\right] = 0 \quad (12b)$$

(c) Continuity Equation

$$\frac{\partial u_{s1}}{\partial s} + \frac{\omega T}{r}\frac{\partial u_{\theta 1}}{\partial \theta} + u_{s1}\left(\frac{1}{r}\frac{dr}{ds} + \frac{1}{h_o}\frac{dh_o}{ds}\right) = 0 \quad (12c)$$

New coefficients in these equations are defined in, Childs (1987).

Solution Procedure: First-Order Equations

The functions $p_{s1}(\theta, t)$, $p_{e1}(\theta, t)$ provide the boundary excitation for the first-order equations. The general form for the excitation takes the form

$$p_{s1}(\theta,t) = e^{j\Omega t}(p_{s1c}\cos n\theta + p_{s1s}\sin n\theta)$$
$$p_{e1}(\theta,t) = e^{j\Omega t}(p_{e1c}\cos n\theta + p_{e1s}\sin n\theta) \quad (13)$$

where n can reasonably be expected to vary from zero (plane wave) upwards through multiples of the number of blades in the impeller. The form of Eq. (13) suggests that the θ variation in boundary pressures is defined in an impeller-fixed coordinate system, which is precessing at the frequency Ω.

The θ and time dependency of the dependent variables is eliminated by assuming the comparable, separation-of-variable, solution format

$$u_{s1} = e^{jf\tau}(u_{s1c}\cos n\theta + u_{s1s}\sin n\theta)$$
$$u_{\theta 1} = e^{jf\tau}(u_{\theta 1c}\cos n\theta + u_{\theta 1s}\sin n\theta)$$
$$p_1 = e^{jf\tau}(p_{1c}\cos n\theta + p_{1s}\sin n\theta) \quad (14)$$

where the coefficients are solely functions of s, and

$$f = \Omega/\omega \quad (15)$$

is the normalized precession frequency. Substituting into Eqs. (12) and equating like coefficients of cos $n\theta$ and sin $n\theta$ yields six first-order equations in s. Introducing the complex variables

$$\bar{u}_{s1} = u_{s1c} + ju_{s1s}, \quad \bar{u}_{\theta 1} = u_{\theta 1c} + ju_{\theta 1s} \quad \bar{p}_1 = p_{1c} + jp_{1s} \quad (16)$$

reduces these real equations to three, complex, ordinary differential equations

$$\frac{d}{ds}\begin{Bmatrix}\bar{u}_{s1}\\ \bar{u}_{\theta 1}\\ \bar{p}_1\end{Bmatrix} + [A(n,f,s)]\begin{Bmatrix}\bar{u}_{s1}\\ \bar{u}_{\theta 1}\\ \bar{p}_1\end{Bmatrix} = 0 \quad (17)$$

where

$$[A] = \begin{bmatrix} B & -jn\omega t/r & 0 \\ A_{3\theta}/u_{s0} & (A_{2\theta} + j\Gamma T)/u_{s0} & -j\dfrac{nb}{ru_{s0}}\left(\dfrac{Ls}{Ri}\right) \\ A_{3s} - Bu_{s0} + j\Gamma T & \left(A_{2s} + j\dfrac{n\omega T}{r}u_{s0}\right) & 0 \end{bmatrix} \quad (18)$$

$$B = \frac{1}{r}\frac{dr}{ds} + \frac{1}{h_0}\frac{dh_0}{ds}, \quad \Gamma = \omega\left(f - n\frac{u_{\theta 0}}{r}\right) \quad (19)$$

Since there is no right-hand side to Eq. (17), the homogeneous solution is the complete solution and can be stated as follows in terms of the transition matrix and initial conditions

$$\begin{Bmatrix}\bar{u}_{s1}\\ \bar{u}_{\theta 1}\\ \bar{p}_1\end{Bmatrix} = [\Phi(n,f,s)]\begin{Bmatrix}\bar{u}_{s1}(0)\\ \bar{u}_{\theta 1}(0)\\ \bar{p}_1(0)\end{Bmatrix} \quad (20)$$

The inlet initial condition $\bar{u}_{\theta 1}(0)$ is set equal to zero, and calculation of $\bar{u}_{s1}(0)$ and $\bar{p}_1(0)$ in terms of the specified boundary conditions is the immediate problem at hand. Substitution from Eqs. (13) and (14) into Eq. (9) yields

$$\bar{p}_{s1} - \bar{p}_1(0) = (1+\xi)\bar{u}_{s1}(0)$$
$$\bar{p}_1(1) - \bar{p}_{e1} = C_{de}u_{s0}(1)\bar{u}_{s1}(1) \quad (21)$$

where

$$\bar{p}_{s1} = p_{s1c} + jp_{s1s}$$
$$\bar{p}_{e1} = p_{e1c} + jp_{e1s} \quad (22)$$

From Eq. (20)

$$\bar{u}_{s1}(1) = \Phi_{11}(1)\bar{u}_{s1}(0) + \Phi_{13}(1)\bar{p}_1(0)$$
$$\bar{p}_1(1) = \Phi_{31}(1)\bar{u}_{s1}(0) + \Phi_{33}(1)\bar{p}_1(0) \quad (23)$$

Hence, from Eq. (21) one obtains

$$\begin{bmatrix} (1+\xi) & 1 \\ \Phi_{31}(1 - C_{de}u_{s0}(1)\Phi_{11}(1) & \Phi_{33}(1) - C_{de}u_{s0}(1)\Phi_{13}(1) \end{bmatrix} \times \begin{Bmatrix}\bar{u}_{s1}(0)\\ \bar{p}_1(0)\end{Bmatrix} = \begin{Bmatrix}\bar{p}_{s1}\\ \bar{p}_{e1}\end{Bmatrix} \quad (24)$$

Inversion of this equation yields

$$\begin{Bmatrix}\bar{u}_{s1}(0)\\ \bar{p}_1(0)\end{Bmatrix} = \begin{bmatrix} Z_{11} & Z_{12} \\ Z_{21} & Z_{22}\end{bmatrix}\begin{Bmatrix}\bar{p}_{s1}\\ \bar{p}_{e1}\end{Bmatrix} \quad (25)$$

$\bar{p}_{s1}$ and $\bar{p}_{e1}$ cannot be specified independently, and a relationship between the two cannot be established without a knowledge of the fluid system beyond the current terminating orifices. For the purposes of this discussion, the arbitrary choice

$$\bar{p}_{s1} = 1, \quad \bar{p}_{e1} = 0$$

is made to examine the influence of pressure perturbations at the impeller exit (annulus inlet). The resulting set of initial conditions for Eq. (20) is then

$$\begin{Bmatrix}\bar{u}_{s1}(0)\\ \bar{p}_1(0)\end{Bmatrix} = \begin{Bmatrix}Z_{11}\\ Z_{21}\end{Bmatrix}, \quad \bar{u}_{\theta 1}(0) = 0 \quad (26)$$

The complete solution along the impeller is found by evaluating Eq. (20) for $s \in [0, 1]$.

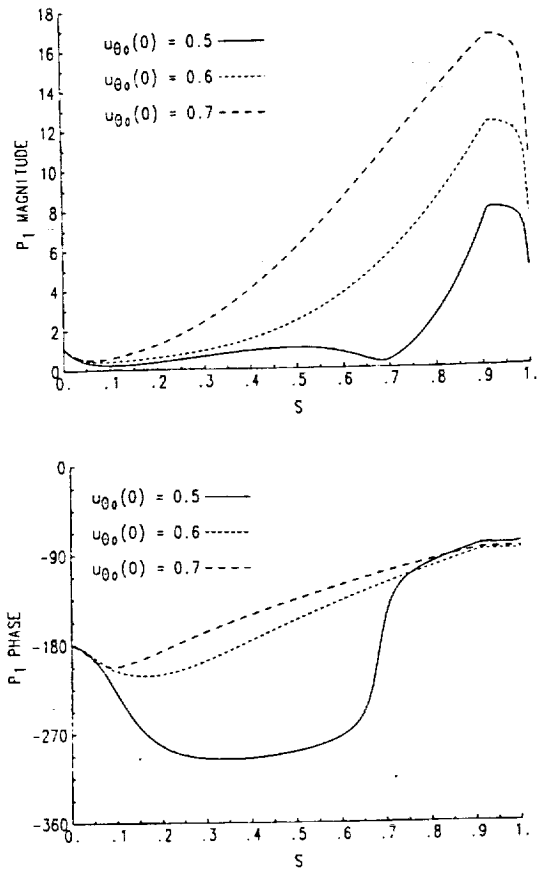

Fig. 4 $\bar{p}_1(s)$ complex eigenvector from Childs (1990b); $n = 1$

Numerical Results. Childs' (1990b) analysis yields complex eigenvalues $\bar{\alpha}$ and eigenvectors $\bar{u}_{s1}(s)$, $\bar{u}_{\theta 1}(s)$, $\bar{p}_1(s)$ for the system modeled by Eq. (12). Figure 4 illustrates the amplitude and phase for the first (lowest-natural-frequency) eigenvalue for $n = 1$; $u_{\theta 0}(0) = 0.5$, 0.6, and 0.7. Observe that the peak-pressure amplitudes lie near the wearing-ring seal, which is consistent with the internally-melted HPFTP wearing-ring-seal results cited earlier. Forced, harmonic-response solutions developed in this study due to impeller-discharge-pressure oscillations also show the largest pressure oscillations to occur near the wearing-ring seal ($s = 0.95$); hence, results presented here focus on $\bar{p}_1(0.95)$. This peak-pressure-oscillation location is very near the exit-wearing-ring seal of Fig. 3. The first question to be addressed here is, "How does $\bar{p}_1(0.95)$ depend on n, f, and C_r?"

Figure 5 illustrates the amplitude and phase of $\bar{p}_1(0.95)$ versus f for $C_r = 0.36$mm, $n = 5$, and $u_{\theta 0} = 0.5$. As will be explained later, the choice $n = 5$, arises because of the number of impeller and diffuser blades used in Bolleter et al.'s (1987) pump. The phase results indicate that numerous resonances exist for positive values of f. However, only the first resonance experiences significant amplification. The remaining fluid modes are heavily damped.

Figure 6 illustrates $|\bar{p}_1(0.95)|$ for $C_r = 0.36$mm, $n = 5$, and $u_{\theta 0}(0) = 0.5$, 0.6, and 0.7. The peak-response frequency increases as $u_{\theta 0}(0)$ is increased from 0.5 to 0.6, and a secondary peak appears around $f = 2.5$. Increasing $u_{\theta 0}(0)$ from 0.6 to 0.7 causes an additional peak to appear.

Figure 7 illustrates $|\bar{p}_1(0.95)|$ for $C_r = 0.36$mm, $u_{\theta 0}(0) = 0.5$, and $n = 0$, 1, 3, 5, and 7. The response is heavily damped for $n = 0$, rises sharply as n is increased to one, but then remains relatively constant as n ranges upwards over 3, 5, and 7. Figure 8 repeats the results of Fig. 7, except for worn clearances; i.e., $C_r = 0.72$mm. Comparisons of Figs. 7 and 8 show that doubling the clearances reduces pressure amplification and

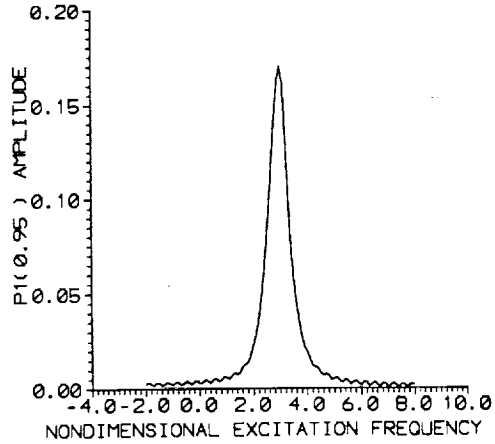

Fig. 5(a) $|\bar{p}_1(0.95)|$ versus f; $C_r = 0.36$mm, $u_{\theta 0}(0) = 0.5$, $n = 5$

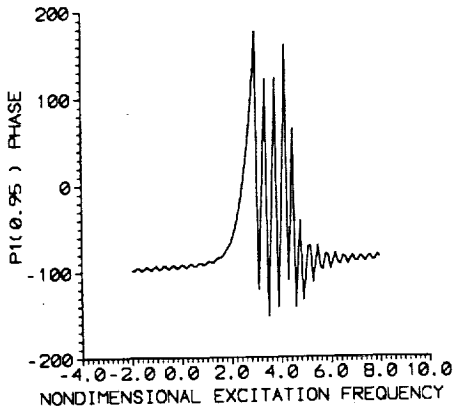

Fig. 5(b) Phase $\bar{p}_1(0.95)$ versus f; $C_r = 0.36$mm, $u_{\theta 0}(0) = 0.5$, $n = 5$

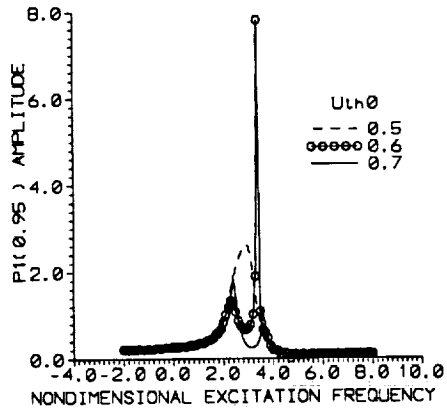

Fig. 6 $|\bar{p}_1(0.95)|$ versus f; $C_r = 0.36$mm, $n = 5$, and $u_{\theta 0}(0) = 0.5$, 0.6, and 0.7

slightly elevates the peak-amplitude-excitation frequency f^*. Table 2 shows f^* versus n for the new($C_r = 0.36$mm) and worn seals($C_r = 0.72$mm). Note that f^* increases more-or-less linearly with increasing n.

The questions which now arise are: **In a real pump, what value of n is likely to arise in impeller-pressure-discharge patterns, and what precession frequency is most likely to be present and dominant?** Answers to these questions have been provided by Bolleter (1988), who presents an analysis for the pressure waves developed by the interaction of impeller and diffuser vanes or impeller vanes and volutes. For an impeller with n_1 vanes and a diffuser with n_2 vanes, Bolleter shows that a rotating pressure wave is developed around the impeller exit with $n = |n_1 - n_2|$ diametral nodes. If $n_1 > n_2$ the pressure wave rotates in the direction of the pump with the frequency $n_1\omega/$

Table 2 f^* (peak-excitation-amplitude frequency) versus n for $u_{\theta 0}(0) = 0.5$

n	1	2	3	4	5	6	7
C_r = 0.36mm	0.3	0.8	1.4	2.1	2.9	3.6	4.2
C_r = 0.72mm	0.3	0.9	1.6	2.4	3.1	3.8	4.4

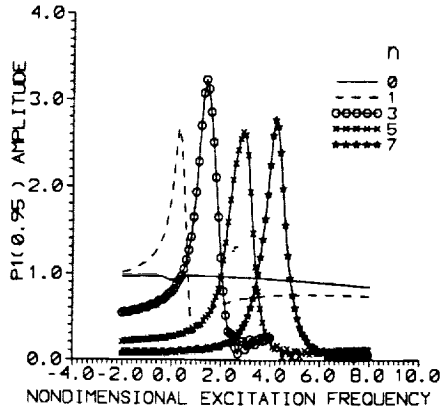

Fig. 7 $|\bar{p}_1(0.95)|$ versus f for n = 0, 1, 3, 5, 7; C_r = 0.36mm, and $u_{\theta 0}(0)$ = 0.5

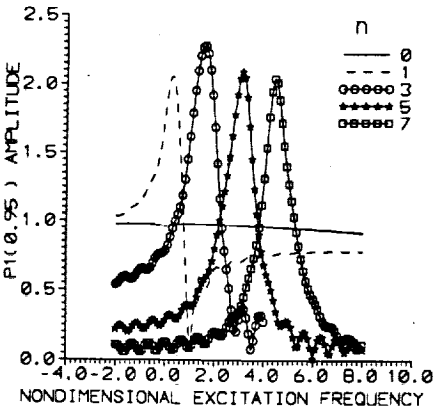

Fig. 8 $|\bar{p}_1(0.95)|$ versus f for n = 0, 1, 3, 5, 7; C_r = 0.72mm, and $u_{\theta 0}(0)$ = 0.5

n. If $n_1 < n_2$ the precessional frequency is $-n_1\omega/n$. Note that n, the number of diametral nodes, cited by Bolleter is the same n used in Eq. (13) for the pressure excitation. Further, in terms of Eq. (13), $\Omega = \pm n_1\omega/|n_1 - n_2|$. Tyler and Sofrin (1962) earlier developed this same result in analyzing the noise generated by the interaction of a rotor and stator in axial compressors of gas turbines.

Bolleter et al.'s pump (1987) used 12 diffuser blades, and the impeller of Fig. 3 has 7 blades. Hence, from Bolleter (1988), $n = |7 - 12| = 5$, and $\Omega = -7\omega/5 = -1.4\omega$. If the impeller were mounted in a double volute, $n = |7 - 2| = 5$, and $\Omega = 7\omega/5 = 1.4\omega$. From Fig. 5 ($n = 5$, $u_{\theta 0}(0) = 0.5$), amplification for $f = -1.4$ and 1.4 is 0.23 and 0.5, respectively. Hence, pressure disturbances from the impeller would generate pressure oscillations about twice as large in a double volute as in a 12-vaned diffuser. However, in either case, because the predominant frequency is well removed from the peak-amplitude-excitation frequency $f^* = 2.9$, impeller pressure disturbances would actually be attenuated by the annulus.

From Bolleter's equations, and the results of Figs. 5 through 7, significant amplification of impeller-discharge-pressure variations will only arise when the number of impeller blades exceeds the number of diffuser (or volute) blades, yielding a positive normalized precession frequency.

$$f^+ = n_1/n = n_1/(n_1 - n_2) \tag{27}$$

Table 3 Dominant normalized precession frequency f^+ and peak-excitation-amplitude frequency f^* versus n_1 and n_2; $u_{\theta 0}(0) = 0.5$

n_1	n_2	n	f^+	f^* (C_r=0.36mm)	f^* (C_r=0.72mm)
8	1	7	1.14	4.2	4.4
	2	6	1.33	3.6	3.8
	3	5	1.60	2.9	3.1
	4	4	2.0	2.1	2.4
	5	3	2.67	1.4	1.6
	6	2	4	0.8	0.9
	7	1	8	0.3	0.3
7	1	6	1.16	3.6	3.8
	2	5	1.40	2.9	3.1
	3	4	1.75	2.1	2.4
	4	3	2.33	1.4	1.6
	5	2	3.5	0.8	0.9
	6	1	7.0	0.3	0.3
6	1	5	1.2	2.9	3.1
	2	4	1.5	2.1	2.4
	3	3	2.0	1.4	1.6
	4	2	3.0	0.8	0.9
	5	1	6.0	0.3	0.3
5	1	4	1.25	2.1	2.4
	2	3	1.67	1.4	1.6
	3	2	2.5	0.8	0.9
	4	1	5.0	0.3	0.3

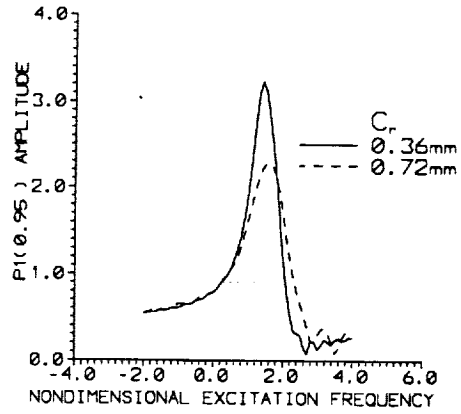

Fig. 9 $|\bar{p}_1(0.95)|$ versus f; n = 3, $u_{\theta 0}(0)$ = 0.5; C_r = 0.36 and 0.72mm

Moreover, for significant amplification within the leakage annulus, f^+ must lie near f^*, the peak-amplitude excitation frequency. Table 3 shows the variation of f^+ and f^* for various combinations of n_1 and n_2. The case of $n_1 = 8$ (eight-bladed impeller) and $n_2 = 4$ (four-bladed diffuser) yields a close proximity of $f^* = 2.1$, 2.4 to $f^+ = 2.0$; however, this is an unrealistic combination. For a practical configuration, the nondimensional frequencies $f^+ = 1.67$ and $f^* = 1.6$ are closest for $n_1 = 5$(five-bladed impeller) and $n_2 = 2$(double-discharge volute). Figure 9 illustrates $|\bar{p}_1(.95)|$ for $u_{\theta 0}(0) = 0.5$ and $n = 3$, confirming the predictions of Table 3. An amplification by a factor of 2.6 is predicted for new clearances and 3.2 for worn clearances.

Numerical Uncertainty. The numerical uncertainty issue for the results presented concerns the numerical integration of Eq. (17). The results presented were obtained with a fourth-order Runge-Kutta integrator package using 200 integration steps for the interval [0, 1]. Repeating these calculations with 400 integration steps yielded the same results to about three significant figures.

Summary and Conclusions

An analysis has been developed and results presented for the pressure oscillations in the leakage annulus between a shrouded pump impeller and its housing. These pressure oscillations are driven by a circumferential variation of the impeller discharge pressure which can precess either in the same or opposite to the direction of rotation. The circumferential variation can be modeled with a Fourier decomposition with each mode having n diametral nodes across the impeller. The peak-pressure oscillations within the impeller are predicted to occur near the exit wearing-ring seal in association with a centrifugal-acceleration-mode response of the fluid within the annulus (Childs, 1988, 1990b). The peak-amplitude-excitation frequency increases linearly with n. Using Bolleter's (1988) work which provides a dependency of n and the precessional frequency on the number of impeller (n_1) and diffuser (n_2) blades, situations are presented which can yield large amplifications (or significant attenuation) of impeller discharge variations. The occurrence and nature of the pressure oscillations are shown to depend on: (*a*) the tangential-velocity ratio of the fluid entering the seal, (*b*) the order of the Fourier coefficient, (*c*) the closeness of the precessional frequency of the rotating pressure field to the first natural frequency of the fluid annulus, and (*d*) the clearance of the wearing-ring seal.

The present results suggest an explanation for the internal melting observed on SSME HPFTP seal parts. However, given liquid hydrogen's significant compressibility, a more complete analysis, including fluid compressibility, is in order.

Bolleter, U., Wyss, A., Welte, Z., and Stürchler, R., 1987, "Measurement of Hydrodynamic Interaction Matrices of Boiler Feedpump Impellers," ASME *Journal of Vibrations, Stress, and Reliability in Design*, Vol. 109, pp. 144-151.

Bolleter, U., 1988, "Blade Passage Tones of Centrifugal Pumps," *Vibrations*, Vol. 4, No. 3.

Childs, D., 1987, "Fluid-Structure Interaction Forces at Pump-Impeller-Shroud Surfaces for Rotordynamic Calculations," *Rotating Machinery Dynamics*, Vol. II, ASME 1987, pp. 581-593.

Childs, D., 1989, "Fluid-Structure Interaction Forces at Pump-Impeller-Shroud Surfaces for Rotordynamic Calculations," ASME *Journal of Vibration, Acoustics, Stress, and Reliability in Design*, Vol. 111, July 1989, pp. 216-225.

Childs, D., 1990a, "Fluid-Structure Interaction Forces at Pump-Impeller-Shroud Surfaces for Axial Vibration Analysis," accepted for publication in ASME *Journal of Vibration and Acoustics*, May 1990.

Childs, D., 1990b, "Centrifugal-Acceleration Modes for Incompressible Fluid in the Leakage Annulus Between A Shrouded Pump Impeller and Its Housing," accepted for publication in ASME *Journal of Vibration and Acoustics*, May 1990.

Hirs, G., 1973, "A Bulk-Flow Theory for Turbulence in Lubricant Films," ASME *Journal of Lubrication Technology*, pp. 137-146.

Tyler, M. J., and Sofrin, T. A., 1962, "Axial Compressor Noise Studies," *SAE Trans.*, Vol. 70, pp. 309-332.